H + CD_4 Abstraction Reaction Dynamics: Product Energy Partitioning†

Wenfang Hu,‡ György Lendvay,§ Diego Troya,# George C. Schatz,*,‡ Jon P. Camden,|| Hans A. Bechtel,||,⊥ Davida J. A. Brown,|| Marion R. Martin,|| and Richard N. Zare||

Department of Chemistry, Northwestern University, Evanston Illinois 60208-3113, Chemical Research Center, Hungarian Academy of Sciences, H-1525 Budapest, P.O. Box 17, Hungary, Department of Chemistry, Virginia Tech, 107 Davidson Hall, Blacksburg, Virginia 24061-0212, and Department of Chemistry, Stanford University, Stanford, California 94305-5080

Received: September 5, 2005; In Final Form: November 12, 2005

This paper presents experimental and theoretical studies of the product energy partitioning associated with the H + CD_4 ($\nu = 0$) → HD + CD_3 reaction for the collision energy range 0.5−3.0 eV. The theoretical results are based on quasiclassical trajectories from (1) first principles direct dynamics calculations (B3LYP/6-31G**), (2) an empirical surface developed by Espinosa-García [*J. Chem. Phys.* **2002**, *116*, 10664] (EG), and (3) two semiempirical surfaces (MSINDO and reparametrized MSINDO). We find that most of the energy appears in product translation at energies just above the reactive threshold; however, HD vibration and rotation become quite important at energies above 1 eV, each accounting for over 20% of the available energy above 1.5 eV, according to the B3LYP calculations. The barrier on the B3LYP surface, though being later than that on EG, predicts significantly higher HD vibrational excitation than EG. This deviation is contradictory to what would be expected on the basis of the Polanyi rules and derives from modest differences in the potential energy surfaces. The CD_3 internal energy is generally quite low, and we present detailed rotational state distributions which show that the CD_3 rotational distribution is largely independent of collision energy in the 0.75−1.95 eV range. The most populated rotational levels are $N = 5$ and 6 on B3LYP, with most of that excitation being associated with motion about the C_2 axes, rather than C_3 axis, of the CD_3 product, in good agreement with the experimental results. Through our extensive studies in this and previous work concerning the scattering dynamics, we conclude that B3LYP/6-31G** provides the best available description of the overall dynamics for the title reaction at relatively high collision energies.

I. Introduction

The H + CH_4 reaction and its isotopic counterparts are benchmark systems for gas-phase polyatomic reactions. Composed of only five light atoms in addition to the carbon atom, the H + CH_4 reaction represents the simplest example of the H + alkane reactions that are important in hydrocarbon combustion. The hydrogen abstraction reaction path, H + CH_4 → H_2 + CH_3, is nearly thermoneutral, $\Delta H(0\ \mathrm{K}) = -9.3 \times 10^{-4}$ eV,[1] and proceeds through a C_{3v} transition state that is 0.64 eV above the reactants according to CCSD(T) calculations (Table 1). Numerous experimental studies have addressed the kinetics of both the forward and reverse reactions,[2−4] but relatively few have provided insight concerning the state-to-state dynamics[5,6] due to the small reaction cross section. For instance at 1.5 eV collision energy, the absolute total cross section is only 0.14 ± 0.03 Å^2.[5]

Extensive theoretical efforts have contributed to the construction of the potential energy surface (PES),[7−15] and calculations of the rate constants and reaction dynamics.[3,16−34] The dynamics techniques employed include quantum dynamics, classical and quasiclassical trajectory methods, direct dynamics, transition state theory, and variants of transition state theory. In 1995, Jordan and Gilbert[12] published a 4-fold symmetric PES (hereafter referred to as JG) based on the functional forms of the Joseph et al. potential.[11] This surface was used in many reduced-dimensionality[20,22−24,28−30] and full-dimensionality[25,26] quantum dynamics calculations to determine thermal rate constants but was found to have important flaws. Espinosa-García then recalibrated this surface with updated kinetic and ab initio data and developed a surface (EG) that is totally symmetric with respect to the methane hydrogens. A quantum instanton approximation calculation[34] utilizing the EG surface obtained rate constants in the 200−2000 K range in good agreement with experiment. After that, Manthe and co-workers[15] proposed a high level ab initio PES that yields rate constants of accuracy comparable to the available experiments. This surface, however, is not globally defined and thus cannot be used in state-resolved dynamics.

Although recent interest has been in the development of various approximate and exact quantum mechanical (QM) scattering calculations, the quasiclassical trajectory (QCT) method still plays a central role in providing valuable dynamical information for polyatomic reactions. Nevertheless, the complete construction of a multidimensional PES for use in dynamical simulations is a demanding task, even for this simplest of six-atom reactions, as it requires high quality electronic structure calculations over a broad range of molecular configurations. In the present study, we emphasize the use of direct dynamics in

† Part of the special issue "Jürgen Troe Festschrift".

* To whom correspondence should be addressed. E-mail: schatz@chem.northwestern.edu.

‡ Northwestern University.

§ Hungarian Academy of Sciences.

Virginia Tech.

|| Stanford University.

⊥ Present address: Department of Chemistry, Massachusetts Institute of Technology, Cambridge, MA 02139.

10.1021/jp055017o CCC: $33.50
Published on Web 12/16/2005

TABLE 1: Saddle Point Properties of H−D′−CD_3 for the PESs and from ab Initio Calculations

parameter	CCSD(T)/CBS//CCSD(T)/cc-pVTZ[c,d]	QCISD(T)/cc-pVTZ[d]	QCISD(T)/6-311G(2d,2p)//MP2/cc-pVTZ	B3LYP/6-31G**	EG	MSINDO[e]	reparametrized MSINDO[e]
R(C−D)/Å	1.0845	1.0846	1.077	1.087	1.094	1.077	1.078
R(C−D′)/Å	1.3965	1.3960	1.409	1.412	1.331[b]	1.272	1.327
R(H−D′)/Å	0.8976	0.8973	0.869	0.894	0.931[b]	0.932	0.834
∠DCD′/°	103.14	103.16	102.7	103.4	107.4	107.1	106.0
∠HD′C/°	180	180	180	180	180	180	180
imaginary frequency/cm^{-1}	1477i	1901i	1609i	1132i	1293i	2261i	720i
ΔE_{barr}[a]/kcal mol^{-1}	14.78 (13.25)	15.10 (13.57)	15.6 (15.2)	9.4 (8.1)	12.9 (12.1)	28.6 (26.1)	15.4 (14.1)
ΔE_{react}[a]/kcal mol^{-1}	2.88 (0.51)	2.90 (0.50)	3.4 (1.1)	1.9 (−1.5)	2.8 (−0.01)	−1.1 (−5.3)	2.8 (−0.8)

[a] Values in parentheses are zero-point corrected energies. [b] The values for r(C−D′) and r(H−D′) at the saddle point reported in ref 13 were misprinted. We thank Prof. J. Espinosa-García for confirming that our values are correct. [c] Energy was calculated using CCSD(T) with complete basis set extrapolation[57] on the CCSD(T)/cc-pVTZ optimized geometry. [d] The comparison of CCSD(T) and QCISD(T) results show that in our system they are identical. [e] We report the vibrational frequencies as obtained using the MSINDO program. Note that the frequencies in MSINDO are scaled so that they are significantly smaller than what would correspond to the actual curvature of the potential surface

studies of the dynamics of the title reaction. Instead of explicitly constructing a global PES, in direct dynamics the PES is implicitly defined by the electronic structure level employed; i.e., energy and forces are computed as the trajectory evolves. The CPU time for calculating energy gradients at each integration point, however, limits the total number of trajectories that can be run, as well as the level of theory that can be utilized. In our direct dynamics study, density functional theory (DFT) calculations based on the B3LYP/6-31G**[35] functional provides the highest level of theory that we have used. For experimental reasons, we have used the isotopic combination H + CD_4.

One of the motivations for this study is that previous theoretical results[7−10,16,20,22] on the reaction dynamics are either old or not directly comparable with the few available experiments,[5,6] which focus on relatively high energies. Despite this, the different studies agree that product translation carries the largest fraction of the total available energy. Some studies also indicate that the H_2 is produced vibrationally cold at low energies, whereas the umbrella mode of CH_3 is more excited.[20,22] In previous work,[36,37] we examined such dynamical properties as the excitation function and product angular and speed distributions for energies spanning the range from 0.5 to 3.0 eV. During the course of this work, we found that the B3LYP PES provided the best agreement with experiment and we proposed a simple model to explain qualitatively the observed trends. The present paper presents a follow-up to that work by examining the role that the various full-dimensional PESs play in determining the product energy partitioning and state distributions for this same system.

Previously, Valentini and co-workers[5] measured the HD product quantum state distributions at 1.5 eV using coherent anti-Stokes Raman spectroscopy (CARS). The HD product was found to be vibrationally cold. Only 7% and 9% of the available energy went to HD vibration and rotation, respectively. This result is noticeably different from what was found in studies of the isoelectronic H + H_2O reaction (also for its isotopic counterpart H + D_2O) at comparable energies, where H_2 (HD) was found to be vibrationally and rotationally more excited in both experiment[38−41] and theory.[40,42,43]

In this study, we record the 2+1 resonance enhanced multiphoton ionization (REMPI) spectra of the nascent CD_3 products that result from the reaction of fast H atoms with CD_4 under single collision conditions. Theoretical calculations of the CD_3 state distributions are then compared with the experimental measurements. The theory is based on quasiclassical trajectories that we have integrated using several PESs: the empirical EG PES,[13] semiempirical surfaces derived from the MSINDO semiempirical method,[44] and a DFT surface based on the B3LYP functional. We also did QCT calculations on the earlier JG surface.[12] The dynamical results, however, are similar to those on EG; thus, only the EG results are presented. In our earlier work,[37] these same surfaces were considered, and it was found that the angular distributions were very sensitive to the potential surfaces. Through a comparison of the calculated integral and differential cross sections with the corresponding experimental quantities, the B3LYP surface provided the best description, even though the B3LYP barrier is ∼0.2 eV lower than that found in high-level ab initio calculations (Table 1). In particular, the product angular distribution on B3LYP was found to be more consistent with stripping dynamics than rebound dynamics at high energy, leading to much more sideways and backward CD_3 scattering than was predicted by other surfaces. It will therefore be of great interest to see how the PES influences the product energy disposal.

II. Experimental Section

The current experimental apparatus has been described in detail elsewhere,[45] and its application to the H + CD_4 system is discussed in our previous work;[37] therefore, only the primary features are described here. Hydrogen bromide (Matheson, 99.999%), methane (Matheson, research grade, 99.999%), and helium (Liquid Carbonic, 99.995%) are mixed in a 1:2:4 ratio in a glass bulb. The resulting mixture is delivered to a pulsed supersonic nozzle (General Valve, Series 9, 0.6 mm orifice, backing pressure ∼700 Torr) and expanded into a high vacuum chamber. The resulting molecular beam enters the extraction region of a Wiley−McLaren time-of-flight (TOF) spectrometer where it is intersected by two laser beams that initiate the reaction and state-selectively probe the products.

Fast H atoms are generated by the UV photolysis of HBr (198−233 nm). After a time delay of 30 ns, the nascent CD_3 reaction products are state selectively ionized using a 2+1 REMPI scheme via the $3p_z{}^2A_2'' \leftarrow X^2A_2''$ transition.[46] The product ions separate according to their mass and are detected by microchannel plates. The 198−233 nm photolysis light was generated by frequency tripling in two BBO crystals the output of a Nd^{3+}:YAG (Continuum PL8020) pumped dye laser (Spectra Physics, PDL3). The ∼330 nm REMPI probe light is generated by frequency doubling in a BBO crystal the output of a Nd^{3+}:YAG (Spectra Physics DCR-2A) pumped dye laser (Lambda Physik, FL2002; Exciton, DCM/LDS698 mix).

When the product REMPI spectra are recorded, the TOF mass spectrometer is operated with large extraction fields (800 V/cm) to collect all the product ions formed in the focal volume of the probing laser. To ensure the measurements are not biased

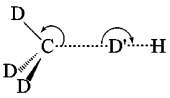

Figure 1. Definition of internal coordinates at the H + $CD_4 \rightarrow$ HD + CD_3 reaction saddle point.

by faster moving products flying out of the probe volume before the slower moving ones, all measurements are made with a time delay between the photolysis and probe laser under conditions that the CD_3 product signal is a linear function of time delay. The optimal photolysis probe time delay was found to be 30 ns, and all REMPI spectra in this study were recorded at this delay. Each collision energy was also recorded under identical experimental conditions (e.g., laser power, focusing conditions, etc.) so that comparisons between them would be meaningful. Spectra were recorded on multiple days and averaged to obtain the final result.

III. Theoretical Details

A. Potential Surfaces. Details of the potential surfaces were given previously[37] so we only summarize them briefly here. The surfaces used are as follows: (1) DFT calculations based on the B3LYP functional with a 6-31G** basis set, (2) the MSINDO semiempirical Hamiltonian (which is a method similar to PM3 but often has better saddle point properties), (3) a reparametrized MSINDO model (hereafter referred to as "reparametrized MSINDO"), in which the values of the C and H parameters in MSINDO have been adjusted for this specific reaction system to make the surface match the stationary point energies and geometries of QCISD(T)/6-311G(2d, 2p)//UMP2/cc-pVTZ calculations, and (4) the EG empirical potential surface. Parameters for the reparametrized MSINDO surface were tabulated in ref 37.

The three important properties of the reaction barriers for abstraction on these surfaces are the barrier height, the H−D′ distance and the C−D′ distance at the saddle point (where D′ represents the abstracted deuterium atom). Table 1 presents these properties for the four surfaces, along with results from high quality electronic structure calculations (the internal coordinates are defined in Figure 1). These results show that the B3LYP surface has the most accurate transition state (TS) geometry, whereas the reparametrized MSINDO surface has the most accurate barrier height when compared to high level ab initio calculations. The MSINDO results are the least accurate. The B3LYP barrier height is ∼0.2 eV too low, which normally would be a likely source of error. Indeed, in the preceding work[37] we saw that at energies close to threshold, B3LYP tends to overestimate reactivity as compared to the other surfaces. Fortunately, the energies relevant to this study are sufficiently high that the error is only a small fraction of the available energy. In fact, B3LYP direct dynamics calculations provide the best description of the experimental reaction cross sections, product speed distributions, and angular distributions. It therefore appears that the B3LYP method better describes the surface for geometries, well away from the minimum energy path (MEP), that are important in determining the higher-energy dynamics. Comparing the TS structures on the four surfaces, we find that the saddle point geometry is more product-like on the B3LYP surface than on either the EG PES or the reparametrized MSINDO PES. For instance, the B3LYP C−D′ distance is ∼0.1 Å longer and the H−D′ distance is ∼0.04 Å shorter than on EG. The reparametrized MSINDO H−D′ distance is ∼0.1 Å shorter than that on EG. In other words, the TSs on both surfaces are later than on the EG PES. The readers are referred to ref 37 for additional information on the stationary point properties of the reaction.

B. Trajectory Calculations. The reagent collision energies explored in our calculations range from 0.5 to 3.0 eV. For EG and MSINDO dynamical calculations, batches of 10 000 trajectories are run at each collision energy. For B3LYP, we have run 100 00 trajectories at 0.75, 1.2, 1.5 and 1.95 eV, respectively, and 1000 at the other collision energies owing to the computational expense involved when using this method. A standard fifth-order predictor, sixth-order corrector integration algorithm[47] is employed to propagate the equations of motion along the trajectory. The integration step for EG and B3LYP is 10.0 au (0.24 fs), and that for the MSINDO calculations is 5.0 au. When generating initial conditions for the polyatomic reactant, we run an intramolecular trajectory starting from the equilibrium geometry of CD_4 but with the kinetic energy corresponding to the zero-point energy (ZPE) in each normal mode. This trajectory is integrated to cover many internal vibrational periods, and the coordinates and momenta of the atoms at each point of integration are saved. When the initial conditions for collision trajectories are calculated, the phase of the vibrational motion is sampled from the saved intramolecular trajectory. In other aspects the standard classical trajectory technology is followed.

When each trajectory is completed, a final analysis is performed to derive various dynamical properties of the products. In particular, we calculate the total angular momentum $\langle L^2 \rangle$ for the CD_3 radical, from which we define the CD_3 rotational quantum number N by using $\langle L^2 \rangle = N(N+1)\hbar^2$. To determine the decomposition of the CD_3 rotational angular momentum relative to body-fixed directions, we propagate the CD_3 coordinates and momenta for an additional 500 (EG, B3LYP) or 1000 (reparametrized MSINDO) steps. At each step we project the CD_3 angular momentum vector onto the instantaneous principal axes, calculate the rotational energy about each axis, and average the results over this period.

In calculating product energy disposal, we subtracted the ZPEs from the vibrational energies of the products. Because we use classical mechanics, the products may have a smaller energy than the ZPE (ZPE violation). In such cases, we "round up" the energies of the fragments to the ZPE values. For a direct dynamics study where only a relatively small number of reactive trajectories are available, this approach is the only computationally practical method that we have available for dealing with the ZPE violation problem. However, in an attempt to assess the significance of our results, we have also considered two other popular approaches in more limited calculations: (1) discarding trajectories that violate the ZPE constraint, and (2) using the Gaussian binning algorithm.

If we discard those trajectories that violate the ZPE constraint, over half the total number of trajectories leading to reaction are omitted. This results in a significant underestimation of the total cross sections; however, in the following we ignore this problem, and simply use the trajectories that do not violate the ZPE constraint (the so-called "good" trajectories) to calculate product energy partitioning information. On the B3LYP surface we had to discard >80% of the reactive trajectories; most of these are due to CD_3 ZPE violation. We found that the average HD internal energy is about the same as if we consider all reactive trajectories, but the average product relative translational energy decreases a lot, and there is a corresponding increase in CD_3 internal energy. However the CD_3 is still largely in its ground state, which means that the net effect of this procedure

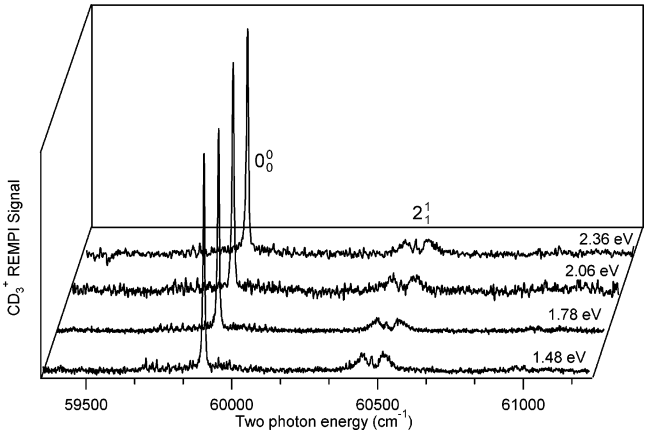

Figure 2. 2+1 REMPI $3p_z \leftarrow X$ spectra of the CD_3 products from the $H + CD_4 \rightarrow HD + CD_3$ reaction as a function of center-of-mass collision energy. The methyl radical products are formed primarily in the ground vibrational state although a small fraction of the products are observed with umbrella bending mode excitation. The state distribution does not change much over the collision energy range studied.

is to reduce the fraction of the total energy in translation, and to increase slightly that in HD internal motion. For example, at 1.5 eV collision energy, the energy fractions in translation, HD vibration, HD rotation and CD_3 internal are 56%, 24%, 20% and 0%, respectively, if we "round up" the average CD_3 internal energy, but when we consider only those "good" trajectories in our analysis (9 out of 83 reactive trajectories), we get 43%, 32%, 15% and 10%. Although these differences are significant, they are not large enough to influence the conclusions from the analysis we provide later. On the EG surface the qualitative picture is largely the same.

Another popular approach is the Gaussian binning procedure,[48,49] which weights trajectories by a Gaussian function centered on the product QM vibrational action. Because only those reactive trajectories with energies near the exact QM vibrational levels contribute significantly, a large ensemble of reactive trajectories are needed to generate statistically meaningful results. Only as a test, we applied Gaussian weighting functions centered on the actions associated with the HD QM vibrational states to the reactive trajectories that we generated on B3LYP and EG. We found that this procedure does not seem to alter the energy disposal much. For example, at 1.2 eV collision energy, the fractions of energy going to translation, HD vibration, HD rotation, and CD_3 internal motion are 65%, 17%, 17%, 0% on B3LYP and 81%, 7%, 6%, 7% on EG. After the Gaussian binning, these quantities become 67%, 17%, 16%, 0% on B3LYP and 80%, 8%, 6%, 6% on EG. We have not calculated the vibrational actions for the CD_3 fragment (which is quite challenging), so we have not studied the effect of Gaussian binning on energy partitioning for that fragment.

IV. Results and Discussion

A. Experimental Results. Figure 2 displays the REMPI spectrum of the CD_3 products in the region of the 0_0^0, 1_1^1, 2_1^1, 2_2^2, and 2_3^1 bands, corresponding to methyl radical fragments in the ground state, or having one quantum of excitation in the symmetric stretch (ν_1), or having one, two or three quanta of excitation in the umbrella-bending (ν_2) mode, respectively. This spectrum is dominated by the large Q-branch members of the 0_0^0 band, but some members of the S and O branches of the 0_0^0 band are also apparent. The 1_1^1 and 2_3^1 bands are found to be absent within the signal-to-noise ratio of our experiment.

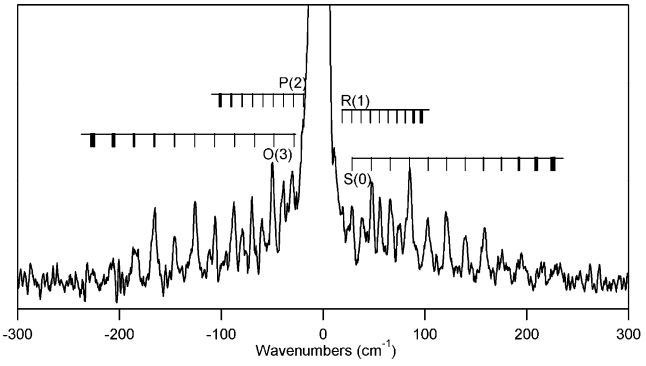

Figure 3. High-resolution scan of the 2+1 REMPI $3p_z \leftarrow X$ CD_3 spectrum in the region of the 0_0^0 band for the reaction $H + CD_4 \rightarrow HD + CD_3$ at $E_{coll} = 1.78$ eV. The O, P, R, and S branch rotational line positions are labeled above the spectrum.

Although a quantitative determination of the internal state distributions is difficult because of the spectroscopy of the $3p_z \leftarrow X$ REMPI transition,[46,50,51] we can draw several qualitative conclusions: (1) the reaction does not significantly populate the energetically allowed symmetric stretch of CD_3 ($\nu_1 = 1$), (2) the major product channels are the ground state and umbrella-bending mode CD_3 ($\nu_2 = 0$, 1), and (3) the CD_3 internal state distribution is largely independent of the collision energy.

Figure 3 displays a high-resolution scan of the 0_0^0 band at $E_{coll} = 1.78$ eV. Although we do not feel that the quality of the spectrum warrants a full fit, we can make several observations. We do not observe rotational levels with $N > 9$ in the spectrum, which indicates that only a small fraction of the total available energy goes into rotational energy of the methyl fragment. It is well-known, however, that the intermediate $3p_z$ Rydberg state of CD_3 suffers from rotational-state-dependent predissociation and lifetime broadening, which is expected to decrease our sensitivity to higher N states.[52] Thus, we cannot rule out a small population in these higher N states. However comparison of the O and S branches, which will be affected unequally by this mechanism, shows reasonable agreement. Therefore, the apparently cold CD_3 rotational distribution is likely due to the state distribution itself and not the spectroscopy of CD_3. We also observe an intensity enhancement of the odd rotational lines over the even ones for the S and O branches, which can be attributed to the population of the low K states of a given N sublevel. The physical interpretation of this result is that the methyl radical rotates preferentially around one of the C_2 axes (tumbling motion), which are directed along a C−D bond, as opposed to the higher symmetry C_3 axis, which is perpendicular to the plane of the molecule (cartwheel-type rotation).

B. Trajectory Results. Figure 4 presents the primary results of our calculations where we display the fractions of energy in translation, f'_{trans}, in HD vibration, $f'_{vib}(HD)$, in HD rotation, $f'_{rot}(HD)$ and in CD_3 internal motion, $f'_{int}(CD_3)$ as a function of the reagent translational energy for the four surfaces that we have considered. In calculating the fractions of the available energy released to HD vibration, and CD_3 internal motion, we subtract the ZPE[53] from the energy of each fragment. Table 2 summarizes selected results from these calculations, including average product internal energies.

Figure 4 shows that the average fraction of energy going to product relative translation decreases with collision energy, whereas the fractions in HD vibration and rotation increase, and CD_3 internal motion receives relatively little of the available energy. At energies barely above threshold, product translation receives more than 90% of the available energy. This behavior

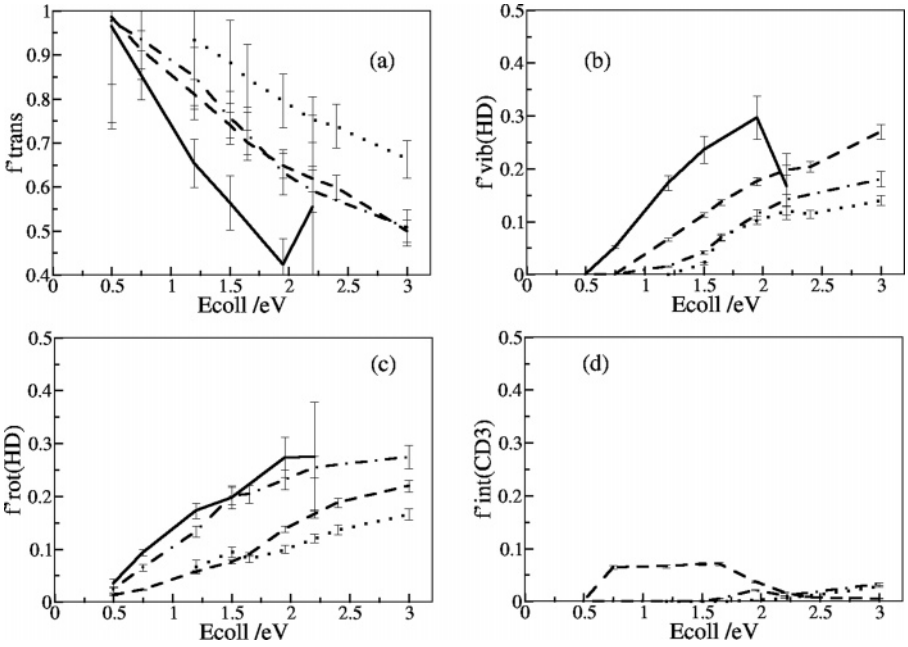

Figure 4. Product energy disposal as a function of center-of-mass collision energy from trajectory calculations. Values are given in terms of the average fractions of the available energy appearing in (a) product relative translation, (b) HD vibration, (c) HD rotation, and (d) CD_3 internal motion for the H + CD_4 ($v = 0$) → HD + CD_3 reaction. Solid lines: B3LYP/6-31G**; dashed lines: Espinosa-Garcia surface; dotted lines: MSINDO PES; dash-dotted lines: reparametrized MSINDO.

TABLE 2: Product Energy Partitioning for the H + CD_4 Abstraction Reaction[53]

E_{coll}, eV		B3LYP/ 6-31G**	Espinosa-García PES	MSINDO	reparametrized MSINDO	expt[5]
0.75	F'_T[a]	85 ± 6% (91 ± 6%)	91 ± 4% (96 ± 5%)		93 ± 9% (100 ± 11%)	
	$f'_{vib(HD)}$[b]	5 ± 0.3% (6.5 ± 0.4)	0% (4.0 ± 0.2)		0% (3.3 ± 0.3[d])	
	$f'_{rot(HD)}$[b]	9 ± 1% (1.7 ± 0.1)	2 ± 0.1% (0.4 ± 0.02)		6 ± 1% (1.4 ± 0.1)	
	$f'_{int(CD_3)}$[b]	0% (12.5 ± 0.8[d])	6 ± 0.3% (14.5 ± 0.7[d])		0% (15.2 ± 1.5[d])	
	% $_{HD(v'=0,1)}$[c]	100 ± 9%	100 ± 6%		100 ± 11%	
1.5	f'_T	56 ± 6% (61 ± 7%)	74 ± 3% (73 ± 3%)	88 ± 9% (100 ± 11%)	76 ± 6% (75 ± 6%)	?% (84%)
	$f'_{vib(HD)}$	24 ± 3% (14.3 ± 1.6)	11 ± 0.5% (9.3 ± 0.4)	2 ± 0.2% (6.9 ± 0.7)	4 ± 0.3% (7.9 ± 0.6)	7% (?)
	$f'_{rot(HD)}$	20 ± 2% (7.3 ± 0.8)	8 ± 0.3% (2.6 ± 0.1)	9 ± 1% (3.7 ± 0.4)	20 ± 2% (6.8 ± 0.5)	9% (?)
	$f'_{int(CD_3)}$	0% (10.9 ± 1.2[d])	7 ± 0.3% (15.8 ± 0.6)	0% (15.5 ± 1.7[d])	0% (16.6 ± 1.3[d])	
	% $_{HD(v'=0,1)}$	78 ± 13%	95 ± 6%	100 ± 14%	99 ± 11%	> 95%
1.95	f'_T	42 ± 6% (45 ± 6%)	65 ± 3% (64 ± 3%)	80 ± 6% (86 ± 7%)	63 ± 5% (62 ± 5%)	
	$f'_{vib(HD)}$	30 ± 4% (19.7 ± 2.7)	18 ± 1% (13.3 ± 0.6)	10 ± 1% (11.1 ± 0.8)	11 ± 1% (11.4 ± 0.9)	
	$f'_{rot(HD)}$	27 ± 4% (13.0 ± 1.8)	14 ± 1% (6.1 ± 0.3)	10 ± 1% (4.9 ± 0.4)	23 ± 2% (10.1 ± 0.8)	
	$f'_{int(CD_3)}$	0% (10.9 ± 1.5[d])	4 ± 0.2% (15.0 ± 0.6)	0.2 ± 0.02% (16.4 ± 1.3)	2 ± 0.2% (18.2 ± 1.5)	
	% $_{HD(v'=0,1)}$	53 ± 13%	84 ± 6%	95 ± 11%	98 ± 12%	

[a] Fraction of the product translational energy in the available energy. Values in parentheses are the percentages of the reagent translational energy channeled into translation of the products. [b] Fraction of HD vibrational energy/HD rotational energy/CD_3 internal energy in the available energy. Values in parentheses are the average HD vibrational energies/HD rotational energies/CD_3 internal energies in kcal/mol. [c] Percentage of the HD products formed in $v' = 0$, 1 vibrational states. [d] The value of the average HD vibrational energy or CD_3 internal energy is below HD or CD_3 zero-point energy.

is consistent with what is expected for a reaction with a late barrier where preferential translational excitation of the products is known to occur. Figure 4a also reveals that the slope of the B3LYP f'_{trans} curve is larger in magnitude than for the rest of the surfaces, which indicates a higher preference for product internal excitation on this surface with increasing translational energy. Also note that the shift of the MSINDO curve toward higher energies reflects the higher barrier on this surface.

Figure 4b shows that the B3LYP f'_{vib}(HD) curve rises from zero at the threshold energy. This curve is shifted downward in energy by ~0.25 eV with respect to the EG and reparametrized MSINDO curves. Therefore, HD is vibrationally more excited on B3LYP than on EG, and even more excited than on the MSINDO surfaces. The TSs on the B3LYP and reparametrized MSINDO surfaces are both later than that on the EG surface (Table 1), but the product energy disposals found on the two surfaces are in sharp contrast to each other, with reparametrized MSINDO predicting less and B3LYP predicting more of the available energy released to HD vibration than does EG, respectively. The reparametrized MSINDO result is in agreement with what is commonly assumed in the Polanyi rule,[54] which states that, for surfaces with later barriers, product vibrational excitation is suppressed, whereas the B3LYP result is not.

To shed light on this behavior, we have examined representative reactive trajectories on the EG, B3LYP and reparametrized MSINDO surfaces. The Supporting Information provides details of the trajectory analysis, including animations of several representative trajectories. Here we summarize the results and describe the correlation between trajectory motion and properties of the surfaces.

First let us examine contours of the PESs as a function of the H−D′ and C−D′ distances. To understand the detailed mechanism, it is necessary to keep in mind that the reaction does not take place on the collinear potential surface; i.e., the

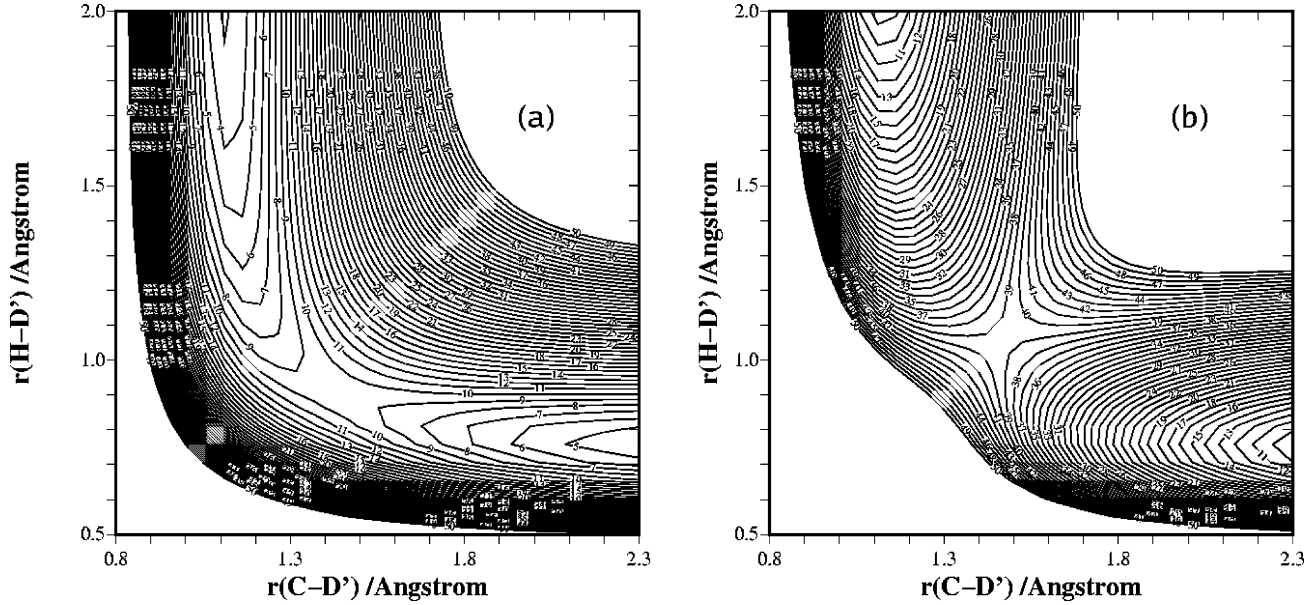

Figure 5. Contours of the B3LYP/6-31G** potential energy surfaces for fixed H−D′−C angles of (a) 180° and (b) 90°. The remaining coordinates are taken to be their TS values. The energy levels are in kcal/mol.

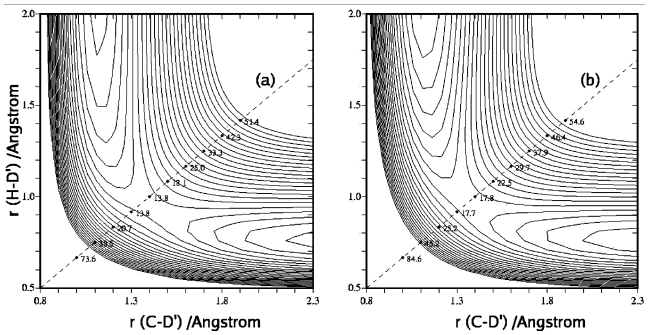

Figure 6. Contours of the (a) B3LYP and (b) EG potential surfaces for a fixed H−D′−C angle of 140°. Energies at the points ($r_{C-D'}$, $r_{H-D'}$) = (1.0, 0.667), (1.1, 0.75), (1.2, 0.833), (1.3, 0.917), (1.4, 1.0), (1.5, 1.083), (1.6, 1.167), (1.7, 1.25), (1.8, 1.333), (1.9, 1.417) are marked in kcal/mol.

H−D′−C angle changes during the course of the collision. Figure 5 presents sections of the B3LYP potential surfaces for H−D′−C bending angles of 180° and 90°. These results show that the saddle point on the bent potential surface is at larger C−D′ and H−D′ separations than on the collinear PES. The EG surface shows somewhat similar contours, as indicated in Figure 6 for a bending angle of 140°, but an important difference between EG and B3LYP is that the repulsive wall is steeper on EG in the corner region where the inner turning points occur (see the Supporting Information). This is apparent from the energies that are given along a specific cut that is plotted in Figure 6, where we see that the difference in energy between EG and B3LYP increases from 0.13 eV to over 0.43 eV in going from the MEP to the inner corner region at a point that is roughly 2.6 eV above the MEP. A consequence of this is that the inner repulsive wall on EG constrains the trajectory to be closer to the MEP, and guides trajectories more efficiently toward products. On the B3LYP PES, trajectories can wander more easily off the MEP and often get reflected back to the reactants before reaching the barrier, which is later than on EG, leading to small reaction cross sections on this surface, especially at higher energies.

Another property of the potential surfaces that plays an important role in the dynamics is the variation of energy with

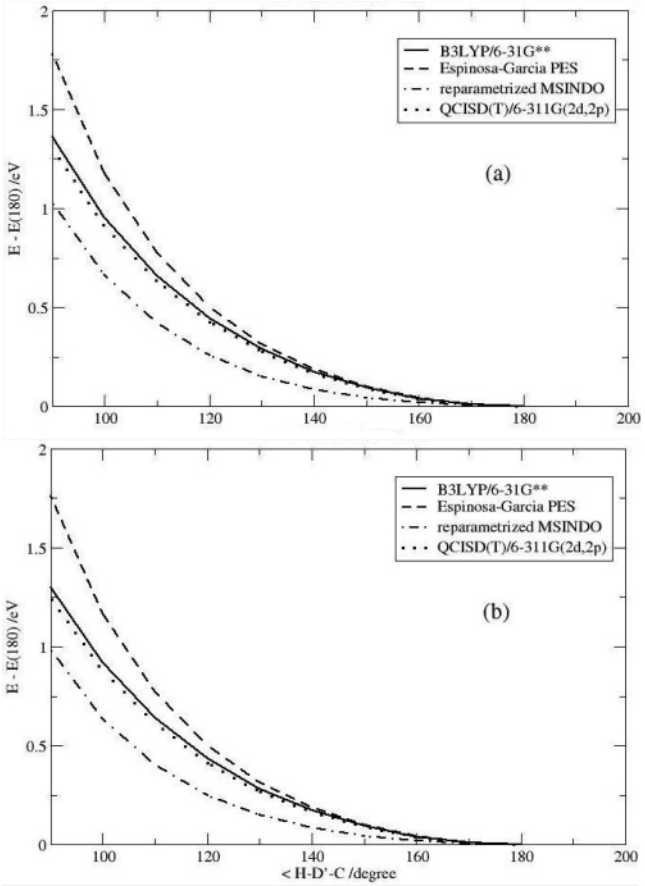

Figure 7. H−D′−C bending-energy curves at the abstraction saddle point: (a) H−D′−C−D dihedral angle = 0°; (b) H−D′−C−D dihedral angle = 180°. Energies are relative to the energy of the TS. The curves depict the dependence of the energy on the H−D′−C angle and the remaining coordinates are fixed at their TS values for the different methods.

H−D′−C bending angle, which is plotted in Figure 7 for the B3LYP, EG and reparametrized MSINDO surfaces for two selected H−D′-C−D dihedral angles, along with results from QCISD(T)/6-311G(2d,2p) ab initio calculations. The figure shows that the EG surface is much more repulsive (i.e., the

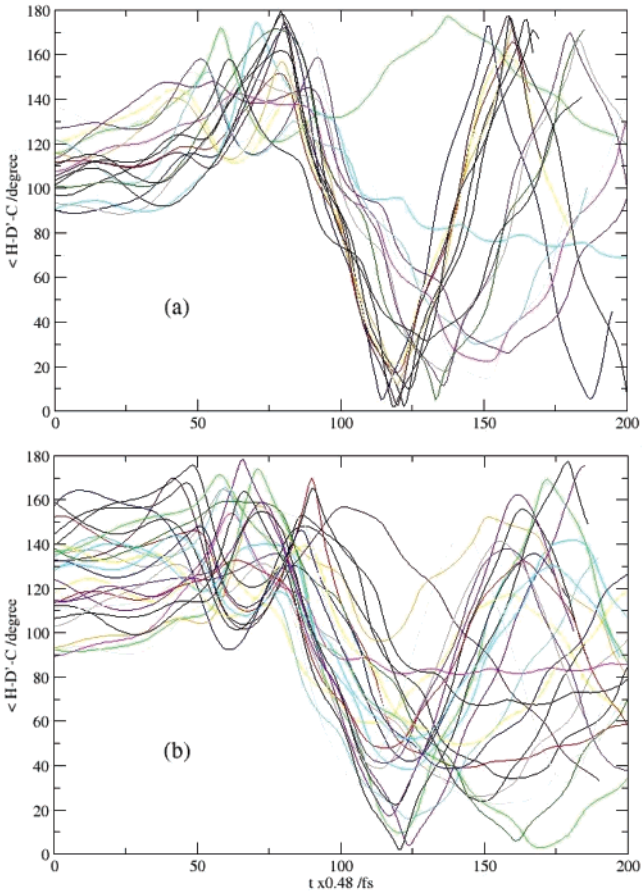

Figure 8. H−D′−C angle versus time for a random selection of large-impact-parameter (b > 1.06 Å) reactive trajectories at 1.95 eV with (a) showing results for B3LYP surface and (b) results for EG.

energy increases the fastest when the H−D′−C angle is bent) than the B3LYP and reparametrized MSINDO surfaces. This result means that the cone of acceptance is wider on B3LYP than on EG. Consequently, the contribution of large impact parameter reactive collisions, in which H attacks in the sideways direction, can be greatly enhanced on B3LYP. Figure 7 also shows that the B3LYP result is the closest to the higher quality QCISD(T) curve, so B3LYP is likelier to provide a more nearly correct description of the dynamics.

We examine how these potential surface properties correlate with results from trajectory calculations. In Figure 8 we plot the H−D′−C bending angle versus step number (the time steps here are 0.48 fs, which is twice the trajectory time step) for reactive trajectories with large impact parameters (b > 1.06 Å) at 1.95 eV on B3LYP and EG. The first inner turning points occur at steps 54−70, so the approach region corresponds to roughly the first 50 steps. In this region we see quite different values for the H−D′−C angles, with average values at $t = 0$ of 124° on EG and 109° on B3LYP. This result clearly demonstrates a wider cone of acceptance on B3LYP. A consequence of this wider cone of acceptance is presented in Figure 9, where we use the calculated opacity functions $P(b)$ to plot $bP(b)$ versus b for a collision energy of 1.95 eV. It is shown that although the overall reaction probability is larger on EG than on B3LYP (a consequence of the earlier barrier location on EG), the reactive region on B3LYP extends to larger impact parameters (b > 2.12 Å). Large impact parameter reactive collisions also contribute more significantly to $bP(b)$ on B3LYP than on EG. This importance of large impact parameter collisions on B3LYP was already noted in refs 36 and 37, where it led to angular

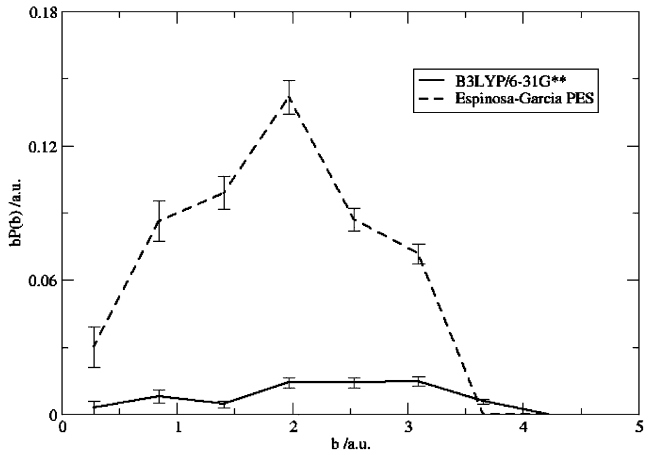

Figure 9. Opacity functions expressed as $bP(b)$ vs b for the B3LYP and EG surfaces at 1.95 eV.

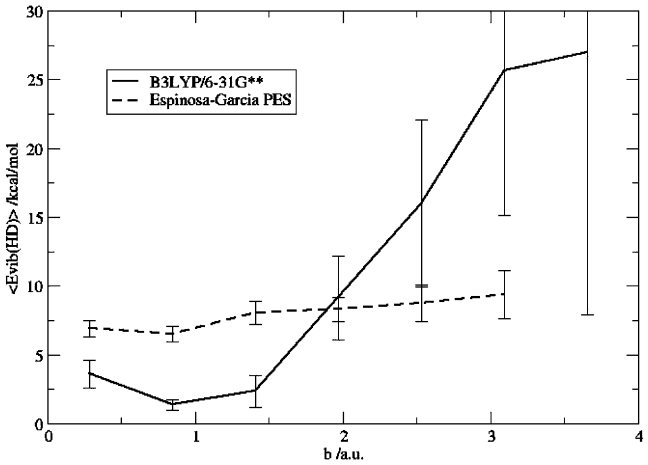

Figure 10. Average HD vibrational energy as a function of impact parameter for the B3LYP and EG potential surfaces.

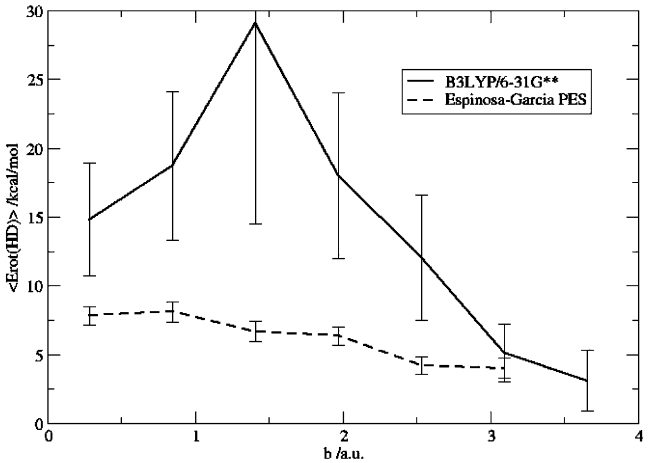

Figure 11. Average HD rotational energy as a function of impact parameter for the B3LYP and EG potential surfaces.

distributions that were more influenced by stripping dynamics than rebound dynamics. Here we show that the large impact parameter collisions also play an important role in the product energy partitioning.

Figures 10 and 11 present average energies deposited in HD vibration and rotation as a function of impact parameter for the B3LYP and EG surfaces. They show that the EG energies are not strongly dependent on impact parameter (increasing or decreasing slowly). However on B3LYP, the HD vibrational

energy increases very rapidly from a value that is below EG at small b to a value that is well above EG at large b. Because the contribution of large b collisions is dominant on B3LYP, HD is vibrationally more excited on B3LYP than on EG. As for HD rotation, although the B3LYP energies decrease rapidly with increasing impact parameter for $b > 0.79$ Å, they largely stay well above the EG result, leading to an average HD rotational energy that is higher than on EG.

The limiting case of large impact parameter collisions should give stripping behavior at high energies, so it is useful to calculate the average energy transfer into internal motions (vibration plus rotation) of HD using a simple kinematic model, in which we assume the CD_3 radical acts as a spectator. An elementary calculation estimates that at 1.95 eV, the average HD internal energy from stripping dynamics should be ~1.3 eV (~30 kcal/mol). This is actually what is obtained when adding the average B3LYP vibrational and rotational energies in Figures 10 and 11 in the large b limit. (In fact, for a few large b trajectories on B3LYP, the HD vibrational energy alone exceeds this limit.) Thus we see that the trajectories on B3LYP are very effective in converting reagent translational excitation into product internal excitation. One factor that contributes to this result is the softer inner repulsive wall on the B3LYP surface (noted earlier in the discussion of Figure 6.) In our examination of the B3LYP trajectories (Supporting Information) we find that reactive trajectories at large b climb up the inner repulsive wall while rounding the corner between reactant and product regions. This motion leads to a bobsled effect that very efficiently converts reagent translational energy to product vibrational excitation. On EG the majority of the large b trajectories more closely follow the MEP because of the steeper inner repulsive wall on this surface. The reparametrized MSINDO surface has much narrower wells in both the reactant and product regions than EG or B3LYP. This makes the inner repulsive wall even steeper than on EG, so the comparison between reparametrized MSINDO and EG is more typical of behaviors predicted by the Polanyi rules.

C. CD_3 Rotational Distributions and Comparisons with REMPI Results. Let us also consider the CD_3 internal energy disposal. We see in Figure 4d that although all of the calculations indicate that less than 10% of the available energy goes to CD_3 internal motion, the different surfaces do not agree. Particularly on the EG surface, $f'_{int}(CD_3)$ increases rapidly until reaching a plateau at 0.75 eV and then gradually decreases at energies above 1.65 eV. The other surfaces show essentially zero values of $f'_{int}(CD_3)$ for energies below 1.5 eV, meaning that the CD_3 energies are below the zero point energy. As a result, CD_3 is more excited on EG than on the other surfaces at low and intermediate energies. (Note that in this regard the JG and EG differ markedly. On the JG surface, we find that the CD_3 energy is below the ZPE at all energies.) ZPE violation is a well-known flaw associated with QCT calculations, but the fact that the calculated CD_3 internal energy is so small at least points to the fact that the average energy available to the CD_3 product is very limited. For the most part, this result is what we find in our experimental measurements of the product state distributions (see discussion in section IV.A), where vibrationally and rotationally cold CD_3 is produced. There are, however, trajectories on the EG, B3LYP, and reparametrized MSINDO surfaces in which the CD_3 internal energy well exceeds the ZPE. By animating such trajectories, we find that the umbrella bending motion receives most of this excitation.. This behavior is to be expected, of course, as the $D_3C-D'-H$ transition state is pyramidal but the equilibrium geometry of CD_3 is planar.

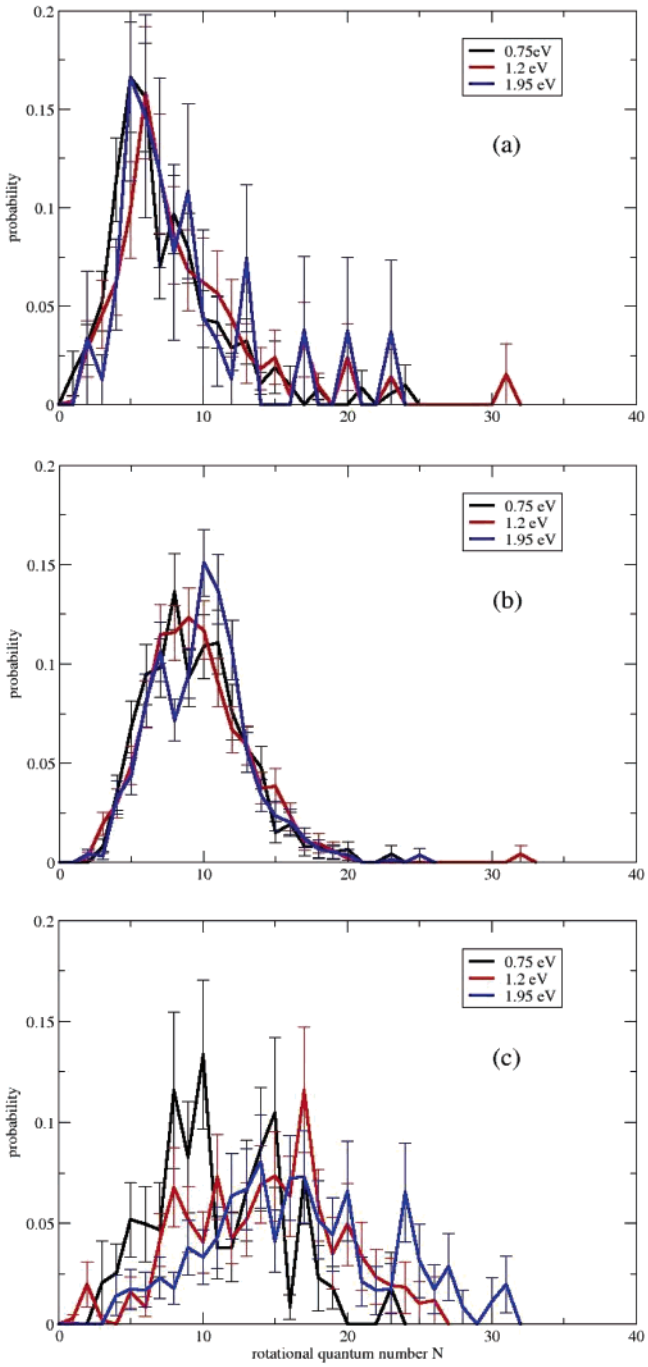

Figure 12. CD_3 rotational states distribution at different collision energies on the (a) B3LYP, (b) EG, and (c) reparametrized MSINDO potential surfaces.

Indeed, umbrella bend excitation is seen in the REMPI spectra. Our trajectory analysis also shows little possibility of CD_3 stretch excitation on these surfaces, which is again in agreement with experiment.

To analyze more deeply the CD_3 internal distribution, we calculate the CD_3 rotational state distributions and compare them with the qualitative picture drawn from experiment. Results for the EG, B3LYP and reparametrized MSINDO surfaces are displayed in Figure 12. It is immediately observed that CD_3 is rotationally the coldest on B3LYP, and hottest on reparametrized MSINDO. On EG and B3LYP, the CD_3 rotational distributions are relatively narrow and peak at $N = 8$, 9, 10 and $N = 5$, 6, respectively. Although the EG and B3LYP distributions are largely independent of the collision energy, the reparametrized

MSINDO distribution broadens and gradually shifts to higher rotational levels as collision energy increases. Irrespective of the higher rotational level tail, the B3LYP results are in best agreement with the experiment, in which it is observed that at 1.78 eV collision energy the methyl radical does not populate states with $N > 9$.

Both experiment and theory also agree that the CD_3 rotates preferentially around the C_2 axes, instead of the higher symmetry C_3 axis. For example, at 1.95 eV the CD_3 rotational energies associated with the two C_2 axes and the C_3 axis (averaged over all reactive trajectories) are 0.020, 0.020, and 0.003 eV on B3LYP, 0.022, 0.019, and 0.011 eV on EG, and 0.057, 0.059, and 0.025 eV on reparametrized MSINDO. This intuitive result appears to be general for H-abstractions from methane as a similar preference for alignment of the methyl rotational angular momentum about the C_2 axes has been observed in both the Cl + CH_4[55] and F + CH_4[51] reactions.

D. Comparison with CARS Experiments. Valentini and co-workers[5] measured the HD product quantum state distributions at 1.5 eV using coherent anti-Stokes Raman spectroscopy. The HD product was found to be vibrationally cold (more than 95% formed in $v' = 0$ and 1). Only 7% of the available energy went to HD vibration and 9% to HD rotation.

Our calculations on B3LYP, however, predict a vibrationally (24%) and rotationally (20%) much hotter HD product. This large discrepancy between the CARS experiment and the B3LYP results is quite unexpected considering the good agreement of B3LYP with the current experiment for other dynamical properties. Actually, the B3LYP results are to a certain extent similar to what was found in studies of the isoelectronic H + H_2O(000) reaction. QCT calculations for that reaction on an accurate PES,[42] which is characterized by a saddle point that is similarly late (O−H′ and H−H′ distances are 1.36 and 0.84 Å, respectively) but much higher in energy (0.94 eV), gave 13% of the available energy going to H_2 vibration, 18% to H_2 rotation and 64% to product translation at a collision energy of 2.2 eV. Experiments done at this energy[38] only determined the sum of H_2 vibration and rotation, but this result, 31%, and the fraction of energy going to translation, 65%, were in excellent agreement with the calculations.

Inspection of the CARS experiment reveals that Valentini and co-workers generated H atoms by photolysis of HI at 266 nm. The H atoms have laboratory translational energies of 1.62 eV (quantum yield = 0.66) and 0.68 eV (quantum yield = 0.34), corresponding to the respective 1.53 ± 0.15 and 0.65 ± 0.10 eV H + CD_4 collision energies. On the basis of trajectory calculations using an early semiempirical PES,[7] they assumed that the reactive cross section at 0.68 eV is negligible compared to that at the higher collision energy. In contrast, our calculations on B3LYP indicate that the reaction cross section is 0.21 Å^2 at 0.65 eV, whereas it is only 0.13 Å^2 at 1.5 eV.[37] Therefore, we suggest that the contribution of the slow channel is not negligible compared to that of the fast channel and the conclusions of the CARS study might need to be reinterpreted.

Because the B3LYP barrier is too low, a possible concern is that our calculation overestimates the role of the reaction of slow H atoms. However, we note that the classical barrier from very high level ab initio calculations, extrapolated to the basis set and correlation energy limits,[13] is 0.58 eV. The zero-point corrected barrier based on this value is 0.52 eV, which is close to the experimental enthalpy of activation at 300 K, 0.50 eV,[56] and about 0.13 eV below the center-of-mass collision energy of the slow channel. In our other work,[37] the experimental reaction cross section was found to decrease with increasing translational energies in the 1.48−2.36 eV range, meaning that the peak reactive cross section must occur at an energy below 1.48 eV. Combining these results and the small absolute cross section at 1.5 eV (only 0.14 ± 0.03 Å^2) given by the measurements of Valentini and co-workers, we estimate that the cross section of the slow channel should not be smaller than one-fourth of that of the fast channel.

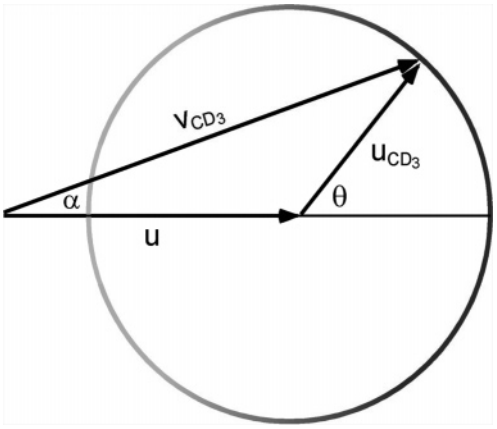

Figure 13. Newton circle showing the vector relationship among u, the velocity of the HCD_4 center of mass, u_{CD_3}, the velocity of CD_3 in the HCD_4 center of mass frame, and v_{CD_3}, the CD_3 lab frame velocity. θ is the center of mass scattering angle, and α is the lab frame scattering angle.

Although the present REMPI experiments do not directly measure the HD product state distributions, we can determine the average HD internal energy by measuring the lab frame anisotropy β_{lab} of the CD_3 coproduct and comparing it to what we calculate on the surfaces. The spatial anisotropy of the product is given by

$$\beta_{lab} = \beta_{phot} P_2(\cos \alpha) \quad (1)$$

where β_{phot} is the photolysis anisotropy parameter, which describes the photofragment angular distribution resulting from photolysis of the precursor HBr or HI molecule with linearly polarized light and takes on values from −1 to +2, $P_2(\cos \alpha)$ is the second-order Legendre polynomial, and α is the angle between $\hat{v}_{CD_3}$ the CD_3 lab frame velocity, and $\hat{u}$, the HCD_4 center-of-mass velocity, as described by the vector relationship shown in Figure 13.

It is clear that for a specific lab frame speed v_{CD_3}, the CD_3 velocity in the center of mass frame, u_{CD_3}, is determined by α and u_{CD_3} relates to the state-to-state energetics ΔE of the reaction through

$$u_{CD_3} = \frac{m_{HD}}{M}\left[\frac{2(E_{coll} - \Delta E)}{\mu'}\right]^{1/2} \quad (2)$$

Here $M = m_{HD} + m_{CD_3}$, and μ' is the reduced mass of the products. Therefore, measurements of the CD_3 lab frame speed and anisotropy for a given CD_3 product state will allow a unique determination of the HD internal energy. However, in practice we can only measure the average anisotropy for a specific lab frame speed, $\beta_{lab}(v_{CD_3})$.

Figure 14 compares the CD_3 lab frame speed distribution and anisotropy as a function of speed from experiment and theory at 1.95 eV. Note that the 1.95 eV experiment has a small contribution from the H atoms that coincide with spin−orbit excited Br (the slow channel); therefore, the theoretical curves are the weighted sum of the slow channel ($E_{coll} = 1.5$ eV) and the fast channel ($E_{coll} = 1.95$ eV).[37] Because we state-selectively

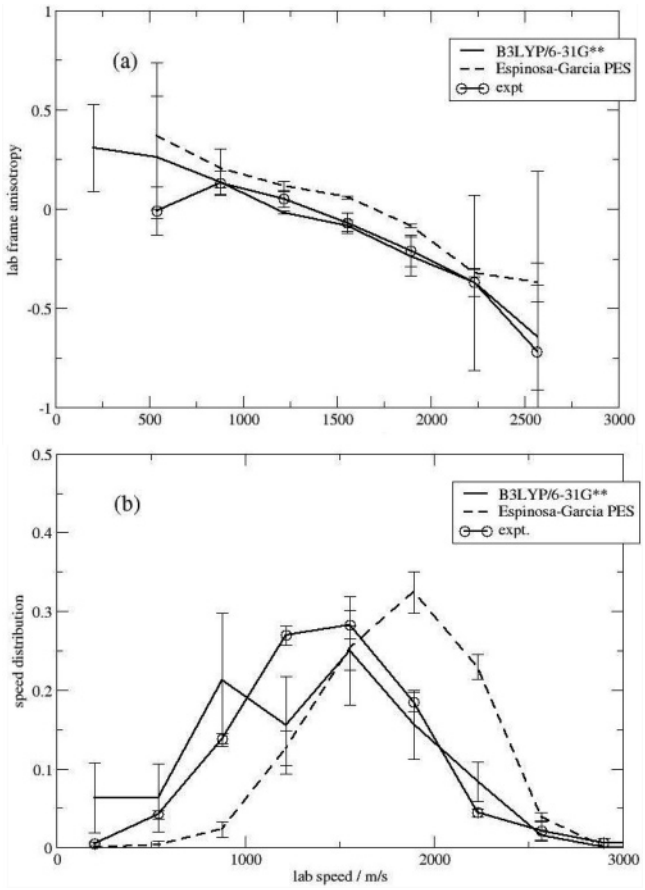

Figure 14. Experimental and calculated (a) CD_3 lab frame anisotropy β_{lab} as a function of speed and (b) CD_3 lab frame speed v_{CD_3} distribution at 1.95 eV.

detect $CD_3(v = 0)$ the speed-dependent anisotropy can be used to estimate the average internal energy deposited in HD for given values of v_{CD_3}.

Figure 14 shows that the B3LYP calculations agree very well with experiment for both the speed distribution and the speed-dependent anisotropy, which suggests to us that the overall energy partitioning scheme predicted by B3LYP should be reliable at least for this collision energy. On EG, the average CD_3 anisotropy is higher, or the average α and, in turn, the average u_{CD_3}, is larger than the experimental measurement in a given speed bin, which translates to smaller HD internal energy. This, when combined with the fact that the EG speed distribution is shifted to higher speeds by several hundreds of m/s with respect to the experimental curve, implies that the HD internal energy predicted by EG is too small compared to the current experimental measurements. We also did measurements at 1.2 eV, and the results show that the B3LYP lab frame anisotropy and speed distribution also agree with experiment within the experimental uncertainty. Thus, we suggest that the estimation of the amount of internal excitation in the HD product determined by Valentini and co-workers is likely to be too low.

V. Conclusions

This paper presents experimental and theoretical results that provide new insights concerning product energy partitioning in the $H + CD_4$ reaction, including one result that departs considerably from what would be expected on the basis of the Polanyi rules: i.e., the saddle point on B3LYP is more product-like than other surfaces examined but leads to higher HD vibrational excitation. This apparent violation results from the wider cone of acceptance around the C−D′ bond on B3LYP as compared to the other surfaces.

We find the B3LYP results are in good agreement with the current experiments, which have examined both the CD_3 state distributions and the average correlated energy in the HD coproduct. This level of agreement between B3LYP direct dynamics calculations and experiment is consistent with that found in our previous study of excitation functions, angular and translational distributions for the title reaction.[37] We believe that, although the B3LYP surface is on relatively low quality electronic structure calculations, this surface provides overall a better description of the surface for regions well away from the minimum energy path, and it is such regions that dominate in the high energy reaction dynamics.

The EG surface represents the best analytical surface currently available for dynamical calculations. However, this PES generates results that generally do not agree with experiment. The reparametrized MSINDO surface is shown to be a marked improvement over the MSINDO surface, and describes the overall dynamics in better agreement with the experiment, but still not as good as B3LYP. This result indicates that the reparametrization process is not sufficiently flexible to rectify all aspects of the fitted surface.

Acknowledgment. J.P.C., H.A.B, and M.R.M. thank the National Science Foundation (NSF) for graduate fellowships. The work at Stanford and Northwestern was supported by the NSF (Grant No. 0242103 and CHE-0131998, respectively). The work at Northwestern was also supported by the Air Force Office of Scientific Research through a Multidisciplinary University Research Initiative (Grant No. F49620-01-1-0335), and by the Missile Defense Agency. G.L. acknowledges support from the Hungarian Academy of Sciences-Hungarian NSF collaboration (Grant No. 71) and the Hungarian NSF (Grant No. T49257).

Supporting Information Available: Details of the trajectory analysis, including animations of several representative trajectories. This material is available free of charge via the Internet at http://pubs.acs.org.

References and Notes

(1) Chase Jr., M. W.; Davies, C. A.; Downey, J. R.; Frurip, D. J.; McDonald, R. A.; Syverud, A. N. *J. Phys. Chem. Ref. Data* **1998**, *14*, Supplement 1.

(2) Shaw, R. *J. Phys. Chem. Ref. Data* **1978**, *7*, 1179. Baulch, D. L.; Cobos, C. J.; Cox, R. A.; Esser, C.; Frank, P.; Just, T.; Kerr, J. A.; Pilling, M. J.; Troe, J.; Walker, R. W.; Warnatz, J. *J. Phys. Chem. Ref. Data* **1992**, *21*, 411. Rabinowitz, M. J.; Sutherland, J. W.; Patterson, P. M.; Klemm, B. R. *J. Phys. Chem.* **1991**, *95*, 674. Marquaire, P. M.; Dastidar, A. G.; Manthorne, K. C.; Pacey, P. D. *Can. J. Chem.* **1994**, *72*, 600. Bryukov, M. G.; Slagle, I. R.; Knyazev, V. D. *J. Phys. Chem. A* **2001**, *105*, 3107.

(3) Sutherland, J.; Su, M.; Michael, J. *Int. J. Chem. Kinet.* **2001**, *33*, 669.

(4) Tsang, W.; Hampson, R. F. *J. Phys. Chem. Ref. Data* **1986**, *15*, 1087. Baeck, H. J.; Shin, K. S.; Yang, H.; Qin, Z.; Lissianski, V.; Gardner, J. *J. Phys. Chem.* **1995**, *99*, 15925. Knyazev, V. D.; Bencsura, A.; Stoliarov, S. I.; Slagle, I. R. *J. Phys. Chem.* **1996**, *100*, 11346.

(5) Germann, G.; Huh, Y.; Valentini, J. *J. Chem. Phys.* **1992**, *96*, 1957.

(6) Camden, J. P.; Bechtel, H. A.; Zare, R. N. *Angew. Chem., Int. Ed.* **2003**, *42*, 5227.

(7) Bunker, D. L.; Pattengill, M. D. *Chem. Phys. Lett.* **1969**, *4*, 315. Bunker, D. L.; Pattengill, M. D. *J. Chem. Phys.* **1970**, *53*, 3041.

(8) Valencich, T.; Bunker, D. L. *Chem. Phys. Lett.* **1973**, *20*, 50. Valencich, T.; Bunker, D. L *J. Chem. Phys.* **1974**, *61*, 21.

(9) Raff, L. M. *J. Chem. Phys.* **1974**, *60*, 2220.

(10) Chapman, S.; Bunker, D. L. *J. Chem. Phys.* **1975**, *62*, 2890.

(11) Joseph, T. R.; Steckler, R.; Truhlar, D. G. *J. Chem. Phys.* **1987**, *87*, 7036.

(12) Jordan, M. J. T.; Gilbert, R. G. *J. Chem. Phys.* **1995**, *102*, 5669.

(13) Espinosa-García, J. *J. Chem. Phys.* **2002**, *116*, 10664.

(14) Wu, T.; Manthe, U. *J. Chem. Phys.* **2003**, *119*, 14.
(15) Wu, T.; Werner, H. J.; Manthe, U. *Science* **2004**, *306*, 2227.
(16) Kuntz, P. J.; Nemeth, E. M.; Polanyi, J. C.; Wong, W. H. *J. Chem. Phys.* **1969**, *52*, 4654.
(17) Schatz, G. C.; Wagner, A. F.; Dunning, T. H. J. *J. Phys. Chem.* **1984**, *88*, 221.
(18) Steckler, R.; Dykema, K. J.; Brown, F. B.; Hancock, G. C.; Truhlar, D. G.; Valencich, T. *J. Chem. Phys*. **1987**, *87*, 7024.
(19) Huang, J.; Valentini, J. J.; Muckerman, J. T. *J. Chem. Phys.* **1995**, *102*, 5695.
(20) Takayanagi, T. *J. Chem. Phys.* **1996**, *104*, 2237.
(21) Kurosaki, Y.; Takayanagi, T. *J. Chem. Phys.* **1999**, *110*, 10830.
(22) Yu, H.-G.; Nyman, G. *J. Chem. Phys.* **1999**, *111*, 3508.
(23) Yu, H.-G.; *Chem. Phys. Lett.* **2000**, *332*, 538.
(24) Wang, M. L.; Li, Y.; Zhang, J. Z. H.; Zhang, D. H. *J. Chem. Phys.* **2000**, *113*, 1802.
(25) Huarte-Larrañaga, F.; Manthe, U. *J. Chem. Phys.* **2000**, *113*, 5115. Huarte-Larrañaga, F.; Manthe, U. *J.* Phys. *Chem. A* **2001**, *105*, 2522.
(26) Bowman, J. M.; Wang, D.; Huang, X.; Huarte-Larrañaga, F.; Manthe, U. *J. Chem. Phys.* **2001**, *114*, 9683.
(27) Pu, J.; Corchado, J.; Truhlar, D. *J. Chem. Phys.* **2001**, *115*, 6266. Pu, J.; Truhlar, D. *J. Chem. Phys.* **2002**, *117*, 1479.
(28) Wang, D.; Bowman, J. M. Bowman. *J. Chem. Phys.* **2001**, *115*, 2055.
(29) Yang, M.; Zhang, D. H.; Lee, S. *J. Chem. Phys.* **2002**, 117, 9539.
(30) Palma, J.; Echave, J.; Clary, D. C. *J. Phys. Chem. A* **2002**, *106*, 8256.
(31) Pu, J.; Truhlar, D. *J. Chem. Phys.* **2002**, *116*, 1468.
(32) Zhang, X.; Yang, G. H.; Han, K. L.; Wang, M. L.; Zhang, J. Z. H. *J. Chem. Phys.* **2003**, *118*, 9266.
(33) Kerkeni, B.; Clary, D. C. *J. Chem. Phys.* **2004**, *120*, 2308.
(34) Zhao, Y.; Yamamoto, T.; Miller, W. H. *J. Chem. Phys.* **2004**, *120*, 3100.
(35) Becke, A. D. *J. Chem. Phys*. **1993**, *98*, 5648. Lee, C.; Yang, W.; Parr, R. G. *Phys. Rev. B* **1988**, *37*, 785.
(36) Camden, J. P.; Hu, W. F.; Bechtel, H. A.; Brown, D. J. A.; Martin, M. R.; Zare, R. N.; Lendvay, G.; Troya, D.; Schatz, G. C. *J. Am. Chem. Soc.* **2005**, *127*, 11898.
(37) Camden, J. P.; Hu, W. F.; Bechtel, H. A.; Brown, D. J. A.; Martin, M. R.; Zare, R. N.; Lendvay, G.; Troya, D.; Schatz, G. C. *J. Phys. Chem. A*, in press.
(38) Jacobs, A.; Volpp, H.-R.; Wolfrum, J. *Chem. Phys. Lett.* **1994**, *218*, 51.
(39) Adelman, D. E.; Filseth, S. V.; Zare, R. N. *J. Chem. Phys.* **1993**, *98*, 4636.
(40) Brouard, M.; Burak, I.; Minayev, D.; O'Keeffe, P.; Vallance, C.; Aoiz, F. J.; Bañares, L.; Castillo, J. F.; Zhang, D. H.; Collins, M. A. *J. Chem. Phys.* **2003**, *118*, 1162.
(41) Brouard, M.; Burak, I.; Marinakis, S.; Rubio Lago, L.; Tampkins, P.; Vallance, C. *J. Chem. Phys.* **2004**, *121*, 10426.
(42) Troya, D.; Gonzalez, M.; Schatz, G. C. *J. Chem. Phys.* **2001**, *114*, 8397.
(43) Zhang, D. H.; Xie, D.; Yang, M.; Lee, S.-Y. *Phys. Rev. Lett*. **2002**, *89*, 283203.
(44) Ahlswede, B.; Jug, K. *J. Comput. Chem.* **1999**, *20*, 563. Jug, K.; Geudtner, G.; Homann, T. *J. Comput.* Chem. **2000**, *21*, 974. Bredow, T.; Geudtner, G.; Jug, K. *J. Comput. Chem.* **2001**, *22*, 89.
(45) Simpson, W. R.; Orr-Ewing, A. J.; Rakitzis, T. P.; Kandel, S. A.; Zare, R. N. *J. Chem. Phys.* **1995**, *103*, 7299.
(46) Hudgens, J. W.; DiGiuseppe, T. G.; Lin, M. C. *J. Chem. Phys.* **1983**, *79*, 571.
(47) *Numerical Recipes in FORTRAN: The Art of Scientific computing*, 2nd ed.; Press, W. H., Flannery, B. P., Teukolsky, S. A., Vetterling, W. T., Eds.; Cambridge University Press: Cambridge, England, and New York, 1992.
(48) Bonnet, L.; Rayez, J. C. *Chem. Phys. Lett.* **1997**, *277*, 183.
(49) Bañares, L.; Aoiz, F. J.; Honvault, P.; Bussery-Honvault, B.; Launay, J.-M. *J. Chem. Phys.* **2003**, *118*, 565.
(50) Black, J. F.; Powis, I. *J. Chem. Phys.* **1988**, *89*, 3986.
(51) Zhou, J.; Lin, J. J.; Shiu, W.; Pu, S. C.; Liu, K. *J. Chem. Phys.* **2003**, *119*, 2538.
(52) Black, J. F.; Powis, I. *J. Chem. Phys.* **1988**, *89*, 3986.
(53) The available energy is calculated as $E_{coll} + \Delta H + ZPE(CD_4) - ZPE(CD_3) - ZPE(HD)$. In cases of ZPE violation, the fractions of the available energy released to the modes that violate the ZPE are set to zero. The available energy is renormalized so that the remaining fractions of energy sum to unity.
(54) Polanyi, J. C.; Wong, W. H. *J. Chem. Phys.* **1969**, *51*, 1439.
(55) Bechtel, H. A.; Camden, J. P.; Brown, D. J. A.; Zare, R. N. *J. Chem. Phys.* 2004, *120*, 5096.
(56) *Evaluated Kinetic Data on Gas-Phase Hydrogen Transfer Reactions of Methyl Radicals*; Kerr, J. A., Parsonage, M. J., Eds.; Butterworth: London, 1976.
(57) Halkier, A.; Helgaker, T.; Jorgensen, P.; Klopper, W.; Koch, H.; Olsen, J.; Wilson, A. K. *Chem. Phys. Lett*. **1998**, *286*, 243.